Am J Transl Res 2024;16(4):1145-1154
www.ajtr.org /ISSN:1943-8141/AJTR0154551

Original Article

Accuracy of mapping results of thoracolumbar vertebral fracture verified using finite element analysis

Hui Lu[1,2,3*], Shuo Han[1,2*], Rong Liu[3,4#], Xuexiao Ma[1#]

[1]Department of Spinal Surgery, The Affiliated Hospital of Qingdao University, Qingdao, Shandong, China; [2]Department of Medicine, Qingdao University, Qingdao, Shandong, China; [3]Institute of Medical Innovation and Transformation, Puren Hospital Affiliated to Wuhan University of Science and Technology, Wuhan, Hubei, China; [4]Department of Orthopedics, Puren Hospital Affiliated to Wuhan University of Science and Technology, Wuhan, Hubei, China. [*]Equal contributors and co-first authors. [#]Equal contributors and co-corresponding authors.

Received November 21, 2023; Accepted March 13, 2024; Epub April 15, 2024; Published April 30, 2024

Abstract: Objective: To verify the results of three-dimensional fracture mapping of T12-L2 compression fractures by the finite element method from a biomechanical point of view, and to provide clinical reference. Methods: This study is a retrospective study. By collecting 150 patients' computerized tomography (CT) data with thoracolumbar compression fractures (T12-L2) with AO type A. Mimics was used for three-dimensional (3D) reconstruction, and 3-Matic was used to mark fracture lines in stereo images. After standardized treatment, all fracture lines were drawn in the same 3D image, and finally fracture lines and fracture map were drawn. Constructing a 3D finite element model of thoracolumbar segment to verify the fracture thermogram results from the perspective of biomechanics. Results: From the fracture map, fracture lines were mainly distributed in the upper part of the vertebral body, the leading edge of the anterior column (AC), and the lateral margin of the middle column (MC). In the finite element analysis, the stress mainly was concentrated on the edge of the anterior and middle column of the vertebral body and the upper part of the vertebral body, and the stress gradually decreased from the upper endplate to the endplate, and the stress was the least in the posterior column (PC) of the vertebral body. Conclusion: The results of finite element analysis further confirm the accuracy of fracture mapping and explain the distribution characteristics of fracture lines. This will provide theoretical support for the selection of clinical fracture treatment, intraoperative implants, and for a standard fracture model.

Keywords: Spinal fracture, thoracolumbar fracture, fracture line distribution, fracture map, finite element analysis

Introduction

Vertebral compression fractures often occur in the thoracolumbar segment (T11-L2), accounting for about 90% of spinal fractures [1]. Kyphosis at the site of spinal fracture can result, and in severe cases, normal work and life quality can be affected [2]. Due to the complex structure and biomechanical mechanism of thoracolumbar injury, it is often difficult to determine its stability after injury, which complicates accurate clinical treatment. Denis et al. [3] proposed the "three-column theory" of the spine by studying the mechanism of spinal injury. Vaccaro et al. [4] proposed the classification theory of thoracolumbar injury, which benefitted diagnosis and surgical planning. Despite their utility, both injury classification theories have disadvantages. However, the damage mechanism was not analyzed from a mechanical point of view in their study.

In recent years, digital orthopedics has led to widespread use of three-dimensional printing technology, finite element analysis (FEA), and fracture map technology by clinical researchers [5, 6]. Among them, fracture mapping shows unique advantages in morphological studies of fracture [7-9]. Fracture mapping, also known as "fracture line distribution mapping", was first proposed by the orthopedic team of the University of Minnesota in 2009. Armitage et al. [10] described the distribution of fracture lines for the first time by describing 90 patients with scapula fracture and superimposing the fracture lines to form a fracture map. Subsequently,

https://doi.org/10.62347/BVDL1541

scholars have applied fracture mapping technology to clinical research. Liu et al. [11] drew fracture lines of 100 patients with intertrochanteric fractures of the femur and spread out the fracture map with map projection technology, clearly showing the frequency of fracture at each part of the proximal femur. By drawing a fracture map, morphological characteristics of fracture line can be visualized, thus providing a new research method for fracture diagnosis, fracture classification, treatment plan selection, surgical fixation design, fracture prone site statistics, and the formulation of a standardized fracture model.

Domestic and foreign studies have been conducted on fracture heat-map, including scapula fracture, proximal humerus fracture [12], radial head fracture [13], distal radius fracture [14], ulna fracture [15], intertrochanteric lateral wall fracture, tibial plateau fracture [16], Pilon fracture [17], posterior malleolus fracture [18], and acetabular fracture [19]. Few studies have applied fracture map projection to the analysis of thoracolumbar fractures. In previous studies, only the phenomenon of fracture occurrence was described, and the reasons for fracture occurrence were not analyzed from the perspective of biomechanics with the method of finite element analysis.

We collected clinical data of 150 patients with T12-L2 compression fractures that were AO type A. Mimics were used for three-dimensional reconstruction, and 3-Matic was used to mark fracture lines in stereo images. After standardized treatment, all fracture lines were drawn in the same three-dimensional image, and finally fracture lines and a fracture map were drawn. A three-dimensional finite element model of the thoracolumbar segment was constructed to verify fracture heat-map results from the perspective of biomechanics.

Materials and methods

In order to better realize our idea, 150 gerontal patients were selected and their CT data of thoracolateral segment were obtained. Of course, these patients were not selected randomly, but were screened according to certain criteria. In order to better understand the situation of these patients, we provide the fracture sites, scan conditions and other information of these patients. Then, three-dimensional reconstruction software was used to draw the fracture mapping, and finite element analysis software was used to establish the thoracolumbar model. We developed a number of indicators to facilitate our understanding of the results.

Inclusion and exclusion criteria

Inclusion criteria: (1) T12-L2 vertebral body type A fracture [20]; (2) patients aged 60-85 years; (3) bone mineral density examination identified patients with osteoporosis; and (4) CT data met the requirements for three-dimensional reconstruction.

Exclusion criteria: (1) CT data cannot meet the requirements of three-dimensional reconstruction; (2) patients with a history of thoracolumbar fracture surgery; (3) comminuted fractures, leading to fracture blocks that cannot be reduced; and (4) abnormal anatomic structure of the thoracolumbar spine.

Materials

This study was a retrospective study. According to inclusion and exclusion criteria, CT data were collected from 150 patients with thoracolumbar compression fractures (T12-L2) that were AO type A from January 2021 to June 2023 at Puren Hospital. Among them, 72 were male and 78 were female, with ages ranging from 60 to 85. There were 51 T12 vertebral fractures, 54 L1 vertebral fractures, and 45 L2 vertebral fractures.

A 65-year-old healthy female volunteer and 150 geriatric patients signed informed consents, and the experimental plan was approved by the hospital ethics committee. Among them, the thoracolumbar CT data of a 65-year-old female volunteer was used to establish a thoracolumbar finite element model. CT data from 150 geriatric patients were used to generate fracture heat-map. So make a distinction between them. A Siemens 64-slice helical CT scanner (Siemens AG, Germany) was used to scan the thoracolumbar vertebral body at 140 kV, 200 mA, and 0.625 mm thickness. CT data were extracted in 512×512 pixel DICOM format.

Fracture heat-map

Step 1: Thoracic and lumbar CT data of 150 patients were imported into Mimics 20.0 (Materialise NV, Leuven, Belgium, 2017) for three-dimensional reconstruction to generate

Table 1. Material properties of the osteoporotic T12-L2 finite element model

Material	Elastic modulus, E (MPa)	Poisson ratio, μ	Stiffness Coefficient	Status
Cortical bone	8040 (67% normal)	0.3	-	Osteoporotic
Cancellous bone	34 (34% normal)	0.2	-	Osteoporotic
Bony endplate	670 (67% normal)	0.4	-	Osteoporotic
Posterior structure	2345 (67% normal)	0.25	-	Osteoporotic
Annulus fibers	455	0.3	-	Normal
Nucleus pulposus	0.4	0.499	-	Normal
Facet cartilage	10	0.4	-	Normal
Anterior longitudinal	20	0.3	33.0	Normal
Posterior longitudinal	70	0.3	20.4	Normal
Interspinous	28	0.3	11.5	Normal
Supraspinous	28	0.8	23.7	Normal
Ligamentum flavum	50	0.3	27.2	Normal
Intertransverse	50	0.3	15.0	Normal

three dimensional stereo images. Then, 3-Matic 12.0 (Materialise NV) software was used to mark the fracture lines and store them.

Step 2: The thoracolumbar CT data of a healthy female volunteer were imported into Mimics for three-dimensional reconstruction as in step 1, and then imported into 3-Matic for smooth processing to obtain three-dimensional reconstruction images of normal thoracolumbar vertebral bone structure as a standard view.

Step 3: Images from 150 patients with fracture lines drawn were registered with the standard view, and then all three-dimensional fracture lines of thoracolumbar fractures were summarized on the same standard view. The aggregated standard view of fracture lines was then transformed into fracture maps. The transformation was based on the frequency of the fracture line of the thoracolumbar spine compression fracture appearing at various positions on the three-dimensional image.

Establishment and analysis of three-dimensional finite element model of the thoracolumbar segment

The three-dimensional model of the thoracolumbar segment of the volunteers in step 2 above was imported into 3-Matic in STL format to process the grid, in which the vertebral body was simulated as cortical bone surrounded by an inner spongy bone core, and the cartilage end plate was covered above and below the disc [21]. The intervertebral disc consists of the annulus fibrosus and the nucleus pulposus, and the cross-sectional area of the nucleus pulposus accounts for 43% of the intervertebral disc cross-sectional area [22]. A solid model was then generated.

In order to simplify the calculation process, only the mechanical properties within the elastic range were considered for bone structure, and an isotropic, uniform, and continuous elastic material model was used to represent the bone structure. According to literature reports [23, 24], specific material parameters were set (**Table 1**).

After material assignment was completed, the lower endplate of the L2 vertebral body was fixed, and loads were applied to the upper endplate of the T12 vertebral body. According to the principle of the three-column theory of the spinal column, the front column and middle column bear 85% load and the back column bears 15% load to distribute the load [25, 26]. A vertical downward load of 400 N and a torque of 7.5 N•m were applied to all models to simulate the thoracolumbar movement under seven states (axial, forward, extension, left bend, right bend, left rotation, and right rotation) (**Figure 1**). Then, the validity of the model was determined [27].

Observational index

According to the three-column theory proposed by Denis in 1983 [3], each vertebral body was divided into AC, MC, and PC. The AC includes the anterior longitudinal ligament, the anterior

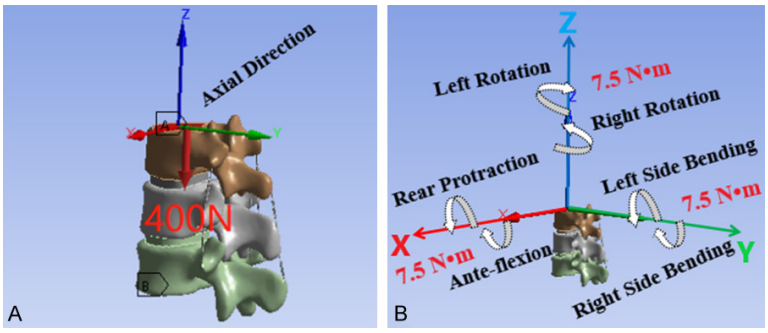

Figure 1. Simulation diagram of boundary conditions and 7 working conditions. A. An axial load of 400 N was applied vertically downwards; B. Six physiological states of the thoracolumbar segment were simulated (anteflexion, rear protraction, left side bending, right side bending, left rotation and right rotation), and 7.5 N•m torque was applied.

half of the vertebral body, and the intervertebral disc. The MC includes half of the vertebral body and intervertebral disc, and the posterior longitudinal ligament. The PC consists of the pedicle, ligamentum flavum, articular process, spinous process, interspinous ligament, and supraspinous ligament. The three-dimensional distribution of fracture lines in the AC, MC, and PC were observed to understand the central tendency of the three-dimensional distribution of fracture lines (**Figure 2**).

T12 was used as the representative vertebral body to observe the stress distribution of a vertebral body in the thoracolumbar segment finite element model under the seven working conditions.

Results

Fracture mapping results were as follows. Because the finite element model was used in the study, the establishment of the finite element model was verified, and the stress distribution characteristics of the thoracolumbar spine in the model were explained.

Analysis of fracture map results

Figure 3 shows the three-dimensional fracture line distribution of the thoracolumbar spine (T12-L2), which intuitively reflects the fracture line distribution characteristics of the three segments. In each vertebra, fracture lines are mainly concentrated in the upper portion, and there are sparse fracture lines in the lower part, forming a sharp contrast from upper to lower. From the side view, fracture lines are mainly concentrated in the AC of each vertebral body; fracture lines in the MC are mainly distributed on both sides of the vertebral body and gradually become sparse; and there are almost no fracture lines in the PC. From the top view, fracture lines are mainly concentrated in the leading edge of the vertebral body and the lateral edge, fanning out, with sparse fracture lines in the middle part of the vertebral body. From the bottom view of each vertebra, there are only a few scattered fracture lines.

Validation results of the model

In this study, the T12-L2 three-dimensional finite element model was loaded under seven working conditions, and the range of motion of joints under various working conditions was measured. The results obtained were highly similar to published findings in the domestic and global literature [25, 28] (**Table 2**), and the finite element model verifies the validity [29].

Finite element analysis of T12 vertebral body

Figure 4 shows the finite element model of the thoracolumbar spine (T12-L2) and the stress distribution view of the T12 vertebral body under axial, forward, and extension working conditions. **Figure 5** shows the stress distribution view of T12 vertebral body under left bend, right bend, left and right rotations. As can be seen from the figure, in six views of the thoracolumbar segment finite element model, the stress gradually decreased from the T12 vertebral endplate to the L2 vertebral lower endplate.

With T12 as the representative vertebra, the stress under the seven working conditions is as follows: axial (25 MPa), forward (74 MPa), extension (73 MPa), left bend (67 MPa), right bend (66 MPa), left rotation (29 MPa), and right rotation (28 MPa). The stress is larger in forward, extension, left bend, and right bend.

From the top view, stress in the axial state is mainly concentrated in the center of the upper endplate of the vertebral body, that is, the posterior part of the AC and the MC. Stress is mainly distributed at the edge of the upper endplate

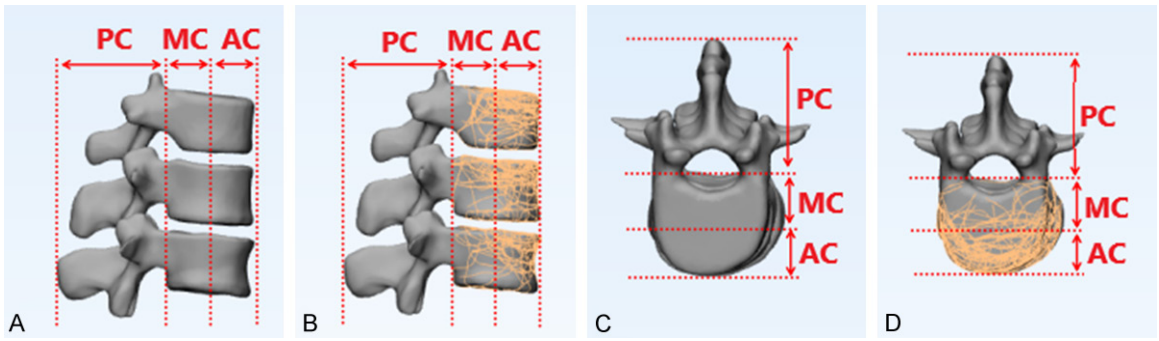

Figure 2. Schematic diagram of three-column theory. A. Area division of three columns in side view of 3D model: AC, MC and PC; B. Area division of three columns in side view of fracture map; C. Area division of three columns in top view of the 3D model; D. Area division of three columns in top view of fracture map.

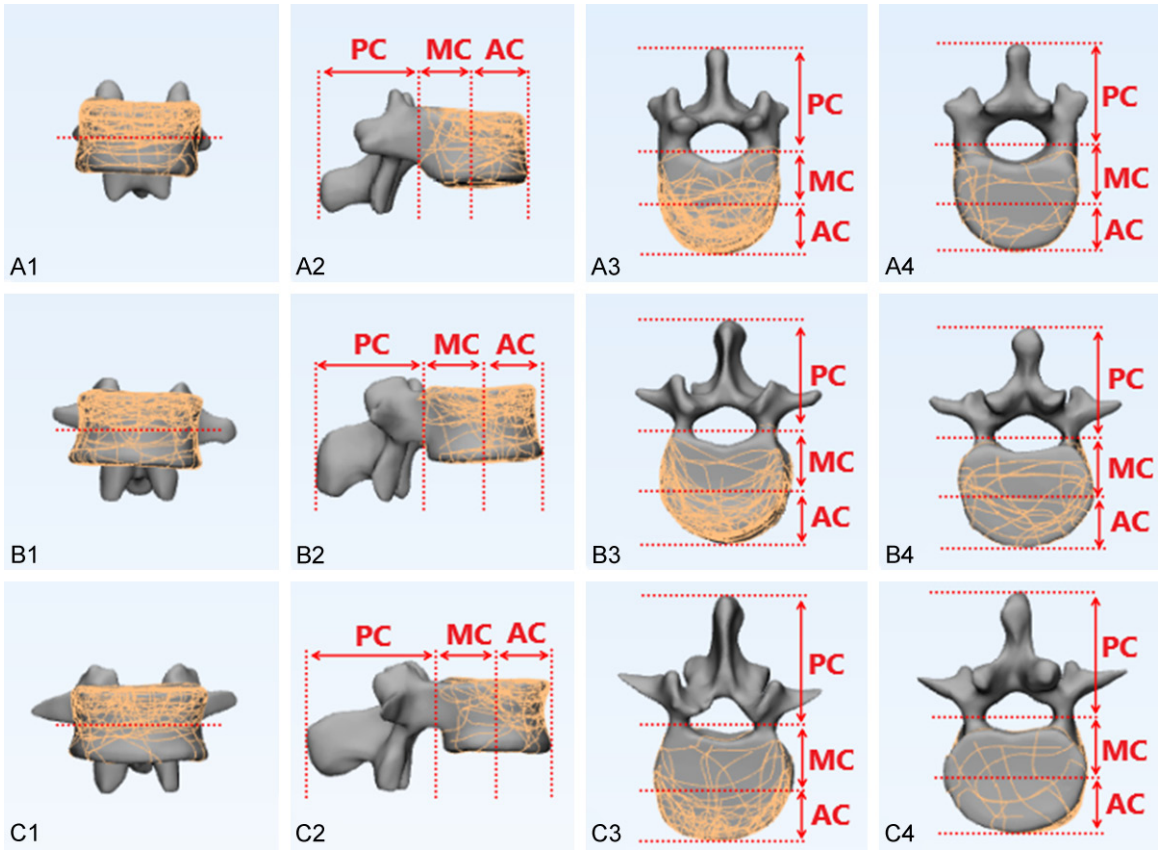

Figure 3. The 3D fracture line distribution of the thoracolumbar spine (T12-L2). (A) is T12 vertebral body view: (A1) Front view; (A2) Side view; (A3) Top view; (A4) Bottom view; (B) is L1 vertebral body view: (B1) Front view; (B2) Side view; (B3) Top view; (B4) Bottom view; (C) is L2 vertebral body view: (C1) Front view; (C2) Side view; (C3) Top view; (C4) Bottom view.

of the vertebral body in forward, extension, and left and right bend states. In the front view, stress is mainly concentrated in the upper part of the anterior vertebral body under the seven working conditions. From the left, right, and bottom views, the stress gradually decreases under the seven working conditions, and the stress on the side of the vertebral body. Stress in the lower part in front of the vertebral body and the bottom of the vertebral body is signifi-

Table 2. Range of motion of finite element model of T12-L2 and comparison with previous research result (°)

Operating Condition	The Present Research	[25]	[28]	The Present OP Model
Ante-flexion	6.8±2.15	7.0	7.9	6.9
Rear Protraction	5.0±1.34	4.5	6.8	4.8
Left Side Bending	5.5±1.75	7.5	7.3	5.7
Right Side Bending	5.3±1.44	-	8.0	5.5
Left Rotation	2.2±1.42	3.1	2.8	2.6
Right Rotation	2.5±1.36	-	3.3	2.7
Axial Direction	-	-	-	-

cantly lower than on the upper endplate in front of the vertebral body. From the rear view, the vertebral body is subjected to the least stress.

In summary, stress was mainly concentrated at the edge of the AC and MC of the vertebral body as well as the upper half of the vertebral body. The stress gradually decreased from the upper endplate to the endplate of the vertebral body, and the stress was lowest in the PC of the vertebral body.

Discussion

By observing the results of fracture mapping and finite element analysis, we clearly know the distribution law of a fracture line. Combining this with finite element analysis, we can see why the fracture line is distributed like this.

Figure 3 shows that fracture lines were mainly distributed in the upper part of the vertebral body, the leading edge of the AC, and the lateral margin of the MC. Therefore, we can infer that the force is mainly concentrated in the upper part of the vertebral body and the AC, which shows a trend of gradually weakening from the AC to the MC and the PC. The tendency is to gradually weaken from the upper endplate of the vertebral body downward. By finite element analysis, stress is mainly distributed at the edge of the upper endplate of the vertebral body in forward, extension, and left and right bend states. Considering the complexity of the actual activity state of the human body, the possibility of fracture is greater with the combination of forward, extension, left bend, and right bend.

From **Figures 4** and **5**, we conclude that stress was mainly concentrated in the center of the vertebral endplate, on back, and in the column part of the AC. This has to do with the Denis three-column theory [3]: stele function directly in maintaining stability, and damage to more than two columns results in unstable fractures. The stress mainly concentrates on the edge of the AC and MC and the upper part of the vertebral body. Stress gradually decreases from the upper endplate to the endplate of the vertebral body, and the stress is lowest in the PC of the vertebral body. This is consistent with the conclusion that fracture lines were mainly distributed in the upper part of the vertebral body, the leading edge of the AC and the lateral edge of the MC in the fracture map. In the fracture map, fracture lines gradually weakened from the upper endplate to the endplate of the vertebral body on the whole, and there were almost no fracture lines in the PC of the vertebral body.

This study has some shortcomings, including: (1) The number of clinical cases included was small, resulting in a certain degree of bias. (2) Only the osseous structure of the thoracolumbar segment was studied, but the surrounding ligaments and posterior structures were not analyzed. In practice, the ligaments and posterior structures around the vertebral body are essential in the stability of thoracolumbar segment. (3) For the structure of each part of the thoracolumbar segment, although it can be simulated by software, there were differences from the real situation. (4) Linear elastic simplified model.

Conclusion

Through finite element analysis, we determined the distribution characteristics of fracture lines in a fracture heat map from the perspective of biomechanics. These data further confirmed the reliability of fracture heat map drawing, and provided a theoretical basis for the occurrence of spinal thoracolumbar fractures in real life.

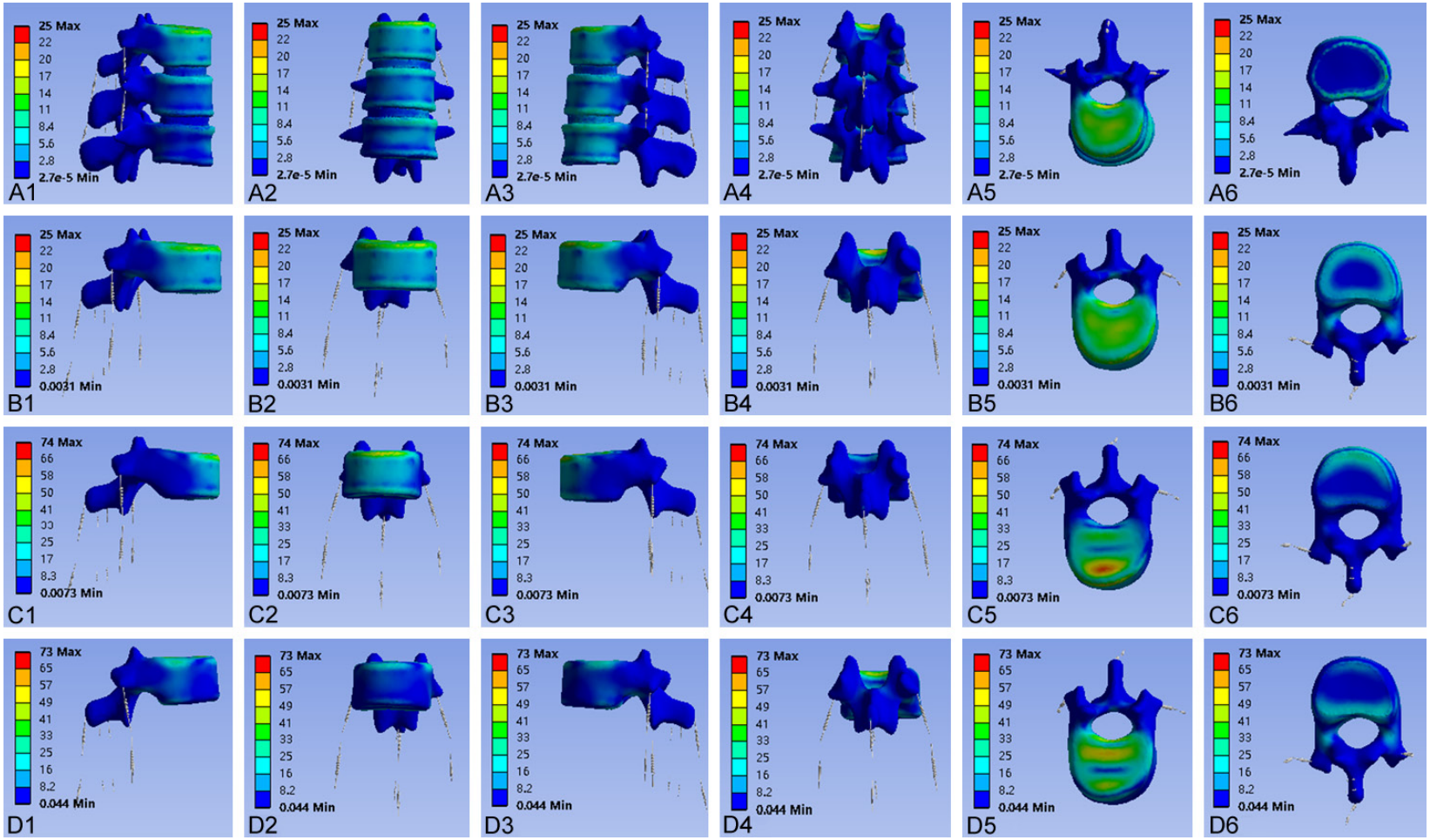

Figure 4. Finite element model of the thoracolumbar spine (T12-L2) and the stress distribution view of the T12 vertebral body under axial, forward, and extension working conditions. (A) is the overall model view of thoracolumbar segment: (A1) Right view; (A2) Front view; (A3) Left view; (A4) Rear view; (A5) Top view; (A6) Bottom view; (B) shows the view of the T12 vertebral body in the axial state: (B1) Right view; (B2) Front view; (B3) Left view; (B4) Rear view; (B5) Top view; (B6) Bottom view; (C) shows the view of T12 vertebral body in the forward state: (C1) Right view; (C2) Front view; (C3) Left view; (C4) Rear view; (C5) Top view; (C6) Bottom view; (D) shows the view of the T12 vertebral body in the extension state: (D1) Right view; (D2) Front view; (D3) Left view; (D4) Rear view; (D5) Top view; (D6) Bottom view.

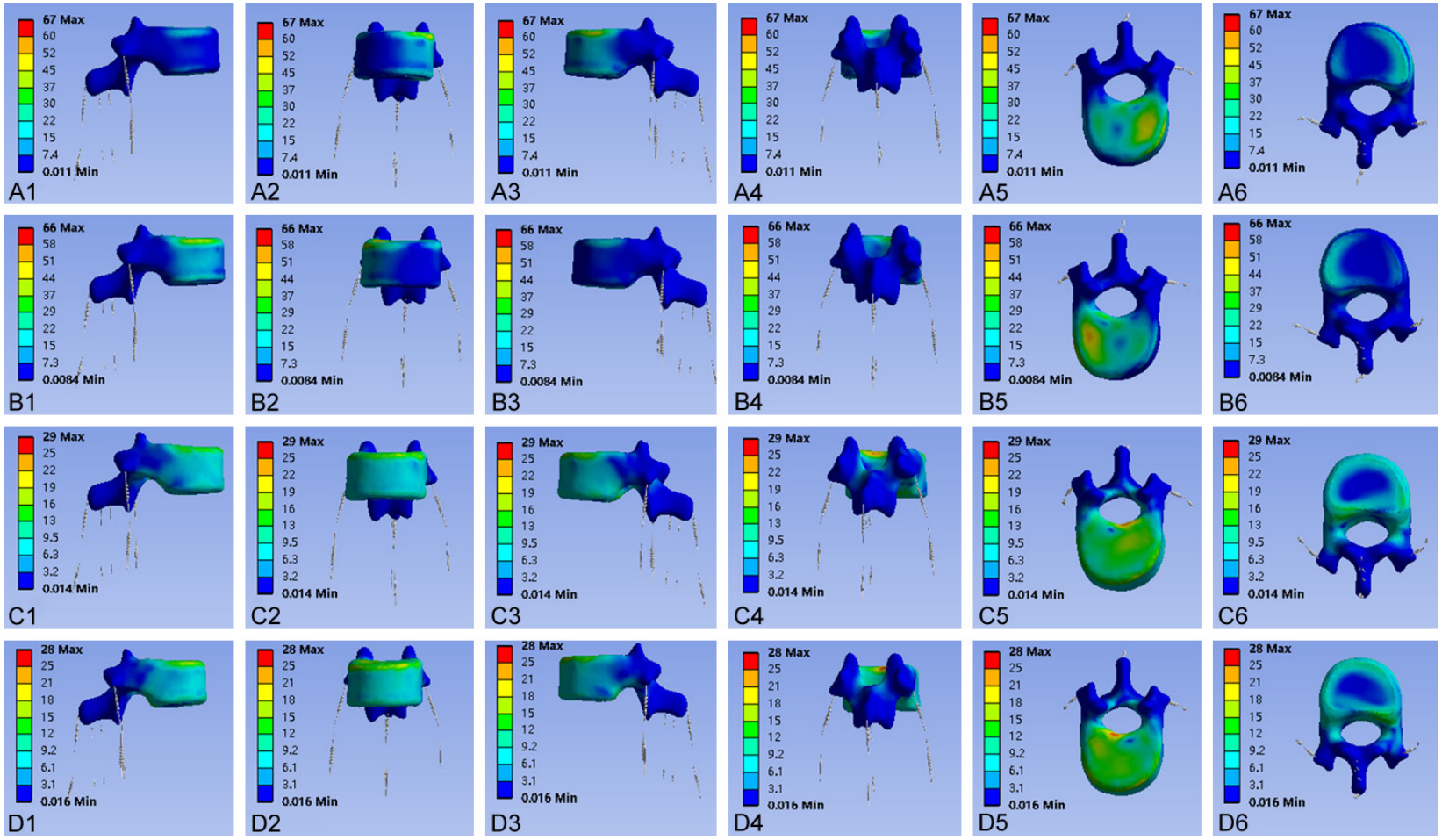

Figure 5. Stress distribution view of T12 vertebral body under left bend, right bend, left and right rotations. (A) shows the view of the T12 vertebral body in the left bend state: (A1) Right view; (A2) Front view; (A3) Left view; (A4) Rear view; (A5) Top view; (A6) Bottom view; (B) shows the view of the T12 vertebral body in the right bend state: (B1) Right view; (B2) Front view; (B3) Left view; (B4) Rear view; (B5) Top view; (B6) Bottom view; (C) shows the view of T12 vertebral body in the left rotation state: (C1) Right view; (C2) Front view; (C3) Left view; (C4) Rear view; (C5) Top view; (C6) Bottom view; (D) shows the view of the T12 vertebral body in the right rotation state: (D1) Right view; (D2) Front view; (D3) Left view; (D4) Rear view; (D5) Top view; (D6) Bottom view.

Our results will provide theoretical support for selecting clinical fracture treatment, the design of intraoperative plans, and the design of a standard fracture model.

Acknowledgements

This work was supported by the Qingdao Science and Technology Benefit the People Demonstration Project (No. 23-2-8-smjk-7-nsh) and 2023 Joint Fund Project of Hubei Key Laboratory of Occupational Hazard Identification and Control (JF2023-K01).

Disclosure of conflict of interest

None.

Address correspondence to: Rong Liu, Institute of Medical Innovation and Transformation, Puren Hospital Affiliated to Wuhan University of Science and Technology, Wuhan, Hubei, China. E-mail: dr_liurong@whu.edu.cn; Xuexiao Ma, Department of Spinal Surgery, The Affiliated Hospital of Qingdao University, Qingdao, Shandong, China. E-mail: maxuexiaospinal@163.com

References

[1] Cahueque M, Cobar A, Zuñiga C and Caldera G. Management of burst fractures in the thoracolumbar spine. J Orthop 2016; 13: 278-281.

[2] Nakashima D, Kanchiku T, Nishida N, Ito S, Ohgi J, Suzuki H, Imajo Y, Funaba M, Chen X and Taguchi T. Finite element analysis of compression fractures at the thoracolumbar junction using models constructed from medical images. Exp Ther Med 2018; 15: 3225-3230.

[3] Denis F. The three column spine and its significance in the classification of acute thoracolumbar spinal injuries. Spine (Phila Pa 1976) 1983; 8: 817-831.

[4] Vaccaro AR, Oner C, Kepler CK, Dvorak M, Schnake K, Bellabarba C, Reinhold M, Aarabi B, Kandziora F, Chapman J, Shanmuganathan R, Fehlings M and Vialle L; AOSpine Spinal Cord Injury & Trauma Knowledge Forum. AOSpine thoracolumbar spine injury classification system: fracture description, neurological status, and key modifiers. Spine (Phila Pa 1976) 2013; 38: 2028-2037.

[5] Lu H, Peng H, Peng Z, Liu D, Wu Q and Liu R. The application of digital design combined with 3D printing technology in skin flap transplantation for fingertip defects during the COVID-19 epidemic. Biomed Res Int 2021; 2021: 5554500.

[6] Misir A, Oguzkaya S, Kizkapan TB, Eken G and Canbaz SB. Fracture line and comminution zone characteristics, and rotator cuff footprint involvement in OTA/AO 11C3-type proximal humeral fractures: complex proximal humerus fracture map. Arch Orthop Trauma Surg 2023; 143: 6219-6227.

[7] Molenaars RJ, Mellema JJ, Doornberg JN and Kloen P. Tibial Plateau fracture characteristics: computed tomography mapping of lateral, medial, and bicondylar fractures. J Bone Joint Surg Am 2015; 97: 1512-1520.

[8] Wang C, Zhu Y, Long H, Lin Z, Zhao R, Sun B, Zhao S and Cheng L. Three-dimensional mapping of distal humerus fracture. J Orthop Surg Res 2021; 16: 545.

[9] Yang Y, Yi M, Zou C, Yan ZK, Yan XA and Fang Y. Mapping of 238 quadrilateral plate fractures with three-dimensional computed tomography. Injury 2018; 49: 1307-1312.

[10] Armitage BM, Wijdicks CA, Tarkin IS, Schroder LK, Marek DJ, Zlowodzki M and Cole PA. Mapping of scapular fractures with three-dimensional computed tomography. J Bone Joint Surg Am 2009; 91: 2222-2228.

[11] Fu Y, Liu R, Liu Y and Lu J. Intertrochanteric fracture visualization and analysis using a map projection technique. Med Biol Eng Comput 2019; 57: 633-642.

[12] Hasan AP, Phadnis J, Jaarsma RL and Bain GI. Fracture line morphology of complex proximal humeral fractures. J Shoulder Elbow Surg 2017; 26: e300-e308.

[13] Mellema JJ, Eygendaal D, van Dijk CN, Ring D and Doornberg JN. Fracture mapping of displaced partial articular fractures of the radial head. J Shoulder Elbow Surg 2016; 25: 1509-1516.

[14] Misir A, Ozturk K, Kizkapan TB, Yildiz KI, Gur V and Sevencan A. Fracture lines and comminution zones in OTA/AO type 23C3 distal radius fractures: the distal radius map. J Orthop Surg (Hong Kong) 2018; 26: 2309499017754107.

[15] Lubberts B, Mellema JJ, Janssen SJ and Ring D. Fracture line distribution of olecranon fractures. Arch Orthop Trauma Surg 2017; 137: 37-42.

[16] Molenaars RJ, Solomon LB and Doornberg JN. Articular coronal fracture angle of posteromedial tibial plateau fragments: a computed tomography fracture mapping study. Injury 2019; 50: 489-496.

[17] PCole PA, Mehrle RK, Bhandari M and Zlowodzki M. The pilon map: fracture lines and comminution zones in OTA/AO type 43C3 pilon fractures. J Orthop Trauma 2013; 27: e152-156.

[18] Mangnus L, Meijer DT, Stufkens SA, Mellema JJ, Steller EP, Kerkhoffs GM and Doornberg JN. Posterior malleolar fracture patterns. J Orthop Trauma 2015; 29: 428-435.
[19] Yang Y, Zou C and Fang Y. Mapping of both column acetabular fractures with three-dimensional computed tomography and implications on surgical management. BMC Musculoskelet Disord 2019; 20: 255.
[20] Magerl F, Aebi M, Gertzbein SD, Harms J and Nazarian S. A comprehensive classification of thoracic and lumbar injuries. Eur Spine J 1994; 3: 184-201.
[21] Lee KK, Teo EC, Fuss FK, Vanneuville V, Qiu TX, Ng HW, Yang K and Sabitzer RJ. Finite-element analysis for lumbar interbody fusion under axial loading. IEEE Trans Biomed Eng 2004; 51: 393-400.
[22] Schmidt H, Heuer F, Simon U, Kettler A, Rohlmann A, Claes L and Wilke HJ. Application of a new calibration method for a three-dimensional finite element model of a human lumbar annulus fibrosus. Clin Biomech (Bristol, Avon) 2006; 21: 337-344.
[23] Rohlmann A, Boustani HN, Bergmann G and Zander T. A probabilistic finite element analysis of the stresses in the augmented vertebral body after vertebroplasty. Eur Spine J 2010; 19: 1585-1595.
[24] Zhang L, Yang G, Wu L and Yu B. The biomechanical effects of osteoporosis vertebral augmentation with cancellous bone granules or bone cement on treated and adjacent non-treated vertebral bodies: a finite element evaluation. Clin Biomech (Bristol, Avon) 2010; 25: 166-172.
[25] Liang D, Ye LQ, Jiang XB, Yang P, Zhou GQ, Yao ZS, Zhang SC and Yang ZD. Biomechanical effects of cement distribution in the fractured area on osteoporotic vertebral compression fractures: a three-dimensional finite element analysis. J Surg Res 2015; 195: 246-256.
[26] Chung SK, Kim YE and Wang KC. Biomechanical effect of constraint in lumbar total disc replacement: a study with finite element analysis. Spine (Phila Pa 1976) 2009; 34: 1281-1286.
[27] Rohlmann A, Zander T, Rao M and Bergmann G. Applying a follower load delivers realistic results for simulating standing. J Biomech 2009; 42: 1520-1526.
[28] Panjabi MM, Kifune M, Liu W, Arand M, Vasavada A and Oxland TR. Graded thoracolumbar spinal injuries: development of multidirectional instability. Eur Spine J 1998; 7: 332-339.
[29] Lu H, Zhang Q, Ding F, Wu Q and Liu R. Establishment and validation of a T12-L2 3D finite element model for thoracolumbar segments. Am J Transl Res 2022; 14: 1606-1615.